

Three-dimensional shape optimization of a centrifugal compressor stage for supercritical carbon dioxide power systems

Special issue paper

Article history:

Submission date: 29 March 2024

Final revision date: 29 July 2024

Acceptance date: 29 October 2024

Publication date: 22 May 2024



*Correspondence:

AR: alessandro.romei@polimi.it

Peer review:

Single blind

Copyright:

© 2025 Romei et al. © This is an open access article distributed under the Creative Commons Attribution License (CC-BY 4.0), which permits unrestricted use, distribution, and reproduction in any medium, provided the original work is properly cited and its authors credited.

Keywords:

shape optimization; two-phase flows; sCO₂; centrifugal compressors; non-ideal effects

Citation:

Romei A., Gaetani P., and Persico G. (2025). Three-dimensional shape optimization of a centrifugal compressor stage for supercritical carbon dioxide power systems. *Journal of the Global Power and Propulsion Society*, 9: 33–44.
<https://doi.org/10.33737/jgpps/195407>

Alessandro Romei^{1*}, Paolo Gaetani¹, Giacomo Persico¹

¹Dipartimento di Energia, Politecnico di Milano, Via Raffaele Lambruschini 4a, 20156, Milano, Italy

Abstract

The design of a centrifugal compressor for supercritical carbon dioxide power cycle must consider non-ideal gas effects and the possible occurrence of two-phase flows. Shape optimization techniques, combined with computational fluid-dynamic (CFD) simulations, can produce optimized designs while inherently coping with such peculiar flow characteristics. This study presents a three-dimensional shape optimization of a compressor stage composed of the impeller and the vaneless diffuser, whose compression starts close to the critical point. Impeller blade angle distributions and meridional channel are parameterized with Bezier control points, enabling local shape control within the optimization routine. The pinch of the vaneless diffuser is also optimized. The experimentally validated CFD solver considers both non-ideal effects and two-phase homogeneous flows, assuming thermodynamic equilibrium and a barotropic fluid. The constrained optimization problem is addressed using genetic algorithms. To mitigate computational costs, Kriging surrogates for the objective function and constraints are trained using a limited number of CFD results. The optimized geometry shows an appreciable efficiency increase (1.1 percentage points) while delivering the design pressure ratio. Although performing better at the design condition, the operating range of the compressor is altered by the optimization. Future optimizations that include both design and off-design operating points in the definition of the objective function and constraints may mitigate this problem.

Introduction

The use of carbon dioxide operating in thermodynamic supercritical conditions (sCO₂) as working fluid in closed gas cycles offers the opportunity to exploit multiple classes of hot sources alternative to fossil fuels, ranging from nuclear energy to concentrated solar power and waste heat from industrial processes. Moreover, sCO₂ power systems also benefit from compactness, thanks to the high density of the working fluid, which ultimately offers the opportunity for effective control of the dynamics of the plant.

A key component of sCO₂ power systems is the main compressor, which is usually centrifugal due to the typical low volumetric flow rates and operates close to the thermodynamic critical point. The corresponding compression process allows for a significant reduction of the work required thanks to the liquid-like properties of CO₂ in these thermodynamic conditions. However, the large departure from the ideal-gas thermodynamics (Pecnik et al., 2012; Baltadjiev et al., 2015; Ameli et al., 2018), as well as the potential occurrence of two-phase flows

(Lettieri et al., 2015; Hosangadi et al., 2022; Toni et al., 2022), pose challenges in the aerodynamic design of impeller blade and meridional channel. The set-up of reliable design tools that comply with the above non-ideal effects is crucial to accelerate the development and the success of the entire technology.

Most of the studies available in the literature analyze the aero-thermodynamics of the flow within the machine or discuss the validation of computational tools for compressor flow analysis (Pecnik et al., 2012; Rinaldi et al., 2015; Ameli et al., 2018; Hosangadi et al., 2019). Only a few works focus on the design process of such non-conventional machines. Lettieri et al. (2012) redesigned a low-flow coefficient centrifugal compressor for carbon capture sequestration (vapor-like CO₂). They increased the outlet impeller blade height to reduce friction losses and added a vaned diffuser to efficiently recover pressure from the resulting more tangential flow. Hacks et al. (2018) designed a laboratory-scale centrifugal compressor. The design strategy was polarized by the small-scale of the machine and the expected high windage loss. Pelton et al. (2018) investigated various design solutions to ensure a wide operating range. Ultimately, they proposed a semi-shrouded impeller with a passive recirculating casing treatment to enhance the surge margin. Romei et al. (2023) revised conventional guidelines applied to sCO₂ centrifugal compressors. They suggested that designing a stage with a flow coefficient smaller than that suggested by standard design practices prevents the occurrence of two-phase flows. All these studies primarily focused on global parameters and overall machine architecture rather than detailed aerodynamic design. To address this, automatic shape optimization methods can bridge the knowledge gap regarding the appropriate design methodology for flow paths and blade shapes.

Optimization methods fall into two categories: gradient-based and gradient-free methods. Gradient-based methods converge quickly but risk getting stuck in local optima. The information of the gradient is acquired by solving adjoint equations; however, it requires a good convergence for both the flow equations and adjoint counterparts to be effective. This requirement may pose challenges in the context of sCO₂ compressors, which are characterized by a complex aerodynamics involving adverse pressure gradients, near-critical thermodynamic conditions, and possible two-phase flows. An alternative is represented by gradient-free methods, which are non-intrusive and explore the global solution space but often converge slowly, making them unsuitable for time-consuming simulations. Evolutionary algorithms, such as genetic algorithms, are a class of gradient-free methods known for their ability to handle noisy and discontinuous objective functions but suffer from slow convergence. To address this, surrogate models, such as Kriging models, are employed to provide predictions for unsampled areas of the design space, allowing for thorough exploration without performing costly simulations. However, surrogate models may offer inaccurate predictions for distant designs from the sampled ones, requiring additional high-fidelity simulations to improve surrogate accuracy (Baert et al., 2020). This integration of surrogate models with evolutionary methods aims to enhance optimization cost efficiency by leveraging surrogate predictions and refining them with additional simulation data.

Examples of evolutionary surrogate-based shape optimization applied to conventional centrifugal compressors are documented by Verstraete et al. (2010) and Hehn et al. (2018). Moving to compressors for supercritical carbon dioxide applications, Romei et al. (2023) did preliminary shape optimizations modifying only the impeller meridional flow path. Recently, Ghimire et al. (2024) addressed the shape optimization of a three-stage axial compressor operating far from the critical point. However, a comprehensive stage optimization, including both meridional flow path and blade angle distribution, for centrifugal compressors operating with carbone dioxide near the critical point is currently lacking.

In the present study, we propose automatic surrogate-based shape optimizations as a means to design sCO₂ centrifugal compressors. The current paper distinguishes itself from our previous work (Romei et al., 2023) by focusing on a specific application and performing systematic shape optimizations of the stage meridional and blade flow path to maximize performance, rather than providing general guidelines. The aim is to determine whether shape optimization can provide additional performance improvements starting from a well-designed stage, achieved through tailored design strategies for this application.

This work is structured as follows: at first, the baseline geometry and the CFD method to estimate compressor performance are introduced. Then, the shape optimization procedure is detailed. The optimized geometries are presented afterwards. Finally, the last section draws some conclusions and delineates prospects for future research works.

Baseline geometry

The baseline machine is a single-stage centrifugal compressor that is designed for the inlet total conditions of $P_{01} = 85$ bar and $T_{01} = 305$ K and has to provide an outlet pressure of ~ 250 bar. These conditions are representative of stationary power systems using supercritical carbon dioxide in a closed cycle. The compressor stage includes a shrouded impeller and a vaneless diffuser. The shrouded architecture is feasible due to the low

peripheral speed (< 220 m/s), which ensures that mechanical stresses remain manageable. The main design parameters are: $\phi_{01} = 0.04$, $\phi_2 = 0.20$, $M_u = 0.70$, and $\lambda = 0.625$, following the design approach proposed by Romei et al. (2023). The impeller has 8 main blades and 8 splitter blades resulting from blade loading considerations. The meridional channel, the blade angle distribution, and the thickness distribution for the main impeller blades are reported in Figure 1. The splitter blade is obtained by cutting the blade angle distributions at a specified normalized meridional coordinate $\tilde{m} = 0.20$ and applying the same thickness distribution as the main blade. The vaneless diffuser extends to $R_4 = 1.6R_2$ (Casey and Robinson, 2021). The mass flow rate is set to 100 kg/s, which is representative of a compressor of a few megawatts. This value is chosen arbitrarily, as it only influences the machine dimensions. Since the machine Reynolds number exceeds 10^8 (using the camber line as the reference length), the geometry obtained by prescribing the above dimensionless parameters can be scaled to different mass flow rates according to the rated power required by the system.

The performance estimates are determined based on steady Reynolds-averaged Navier-Stokes (RANS) simulations. The RANS equations are solved with the Ansys-CFX finite-volume flow solver, using high-order numerical schemes for both inviscid and viscous fluxes. Turbulence effects are introduced by resorting to the $k - \omega$ SST model assuming a fully turbulent flow.

A specific feature of the present model refers to the representation of the non-ideal thermodynamics of the fluid. This is crucial for the proper modeling of turbomachinery operating with sCO₂, whereby the proximity to the critical point originates a large departure from ideal-gas behavior. On top of that, the challenges of simulating the flow in technically-relevant sCO₂ compressors are also related to two-phase flows: the proximity of the inlet compressor state to saturation might trigger phase change processes that need to be taken into account in the simulation model. In this work, we make use of a barotropic model, which belongs to the class of homogeneous equilibrium models (HEM), in which the thermo-physical properties (density and dynamic viscosity) of the fluid are assumed only depending on pressure. The barotropic relationships $\rho = \rho(P)$ and $\mu = \mu(P)$ are generated along the inlet isentrope, $s_1 = s(P_{01}, T_{01})$. These relationships are discretized with a pressure step of 0.05 bar to create look-up tables. These tables are used in the CFD solver to efficiently retrieve thermodynamic properties during the simulation. The present barotropic flow model was validated against experimental data of a megawatt-scale sCO₂ centrifugal compressor prototype in Toni et al. (2022).

Calculations are performed assigning the total pressure at the inlet. The flow rate is imposed at the outflow, except close to choked-flow conditions, for which an average static pressure is assigned. No-slip boundary conditions are imposed on the solid walls. As the flow domain is rotating with the impeller, a counter-rotating velocity is assigned at the endwalls of the vaneless diffuser. Considering the high Reynolds number ($\sim 10^8$), as a consequence of the low kinematic viscosity of carbon dioxide in supercritical conditions, the assumption of hydraulically smooth surfaces is not appropriate and, hence, wall roughness ($k_s = 5$ μm) and corresponding wall functions are specified.

The computational mesh is generated with Ansys-Turbogrid. To reduce the computational cost per simulation, which is critical in shape optimization tasks, periodic boundary conditions are exploited. Therefore, the computational domain includes a single-blade passage containing the main blade, the splitter blade, and the vaneless diffuser. Other components, such as the volute and the sealings, are omitted to reduce the computational cost. The first-layer cell distance is comparable with the roughness to exploit the dedicated wall functions.

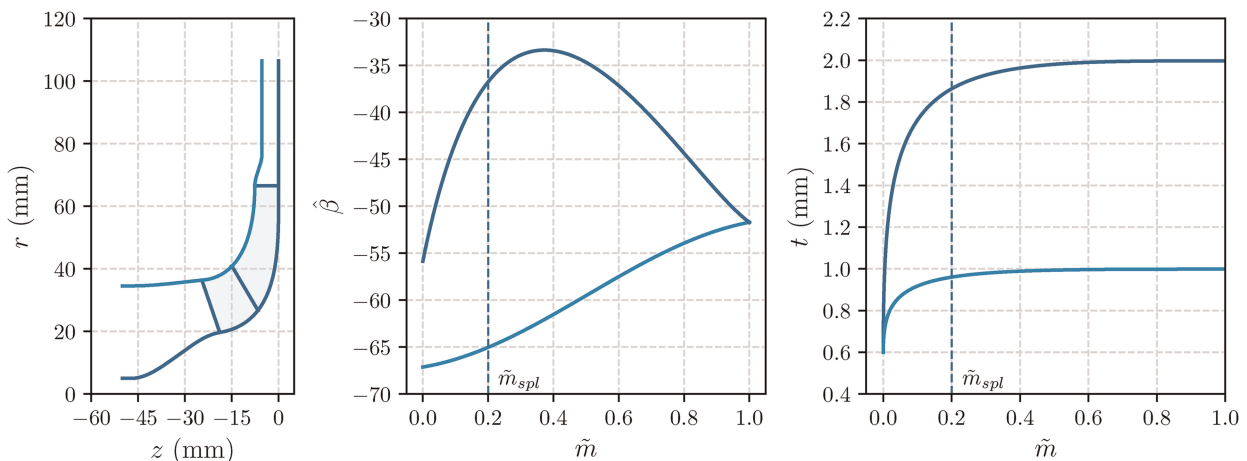


Figure 1. Baseline impeller geometry: (left) meridional view; (middle) blade angle distribution (measured from the meridional direction, positive with rotational speed); (right) thickness distribution.

Starting from a coarse mesh composed of 0.9 million elements and doubling the number of elements each time (with the same mesh topology), a grid convergence analysis is conducted, and the results are illustrated in Figure 2. The grid convergence index is evaluated by taking the first three meshes, yielding a Richardson extrapolated efficiency that differs by less than 0.01% from the value obtained with the finest grid (7.7 million cells). The resulting grid convergence index for the total-to-total efficiency η_{TT} is 0.3% for the medium mesh, composed of 1.9 million cells, which is ultimately selected for the shape optimization.

For the baseline geometry, the CFD simulation returns a $\eta_{TT} = 92.2\%$, $\lambda = 0.625$, and an outlet total pressure of 266 bar. The static pressure is 239 bar with $\eta_{TS} = 79.2\%$.

Shape optimization

Shape parameterization

To perform the shape optimization, the baseline geometry has to be parameterized with a finite number of control points, which become the design variables. This task is accomplished by parameterizing the meridional channel and the blade angle distribution with Bezier control points as in Figure 3. Four control points are used to reproduce the meridional hub contour $\{M_{hj}\}$, the meridional shroud contour $\{M_{sj}\}$, the hub blade angle distribution $\{B_{hj}\}$, and the shroud blade angle distribution $\{B_{sj}\}$, with $j = 1, \dots, 4$. Not all these design parameters

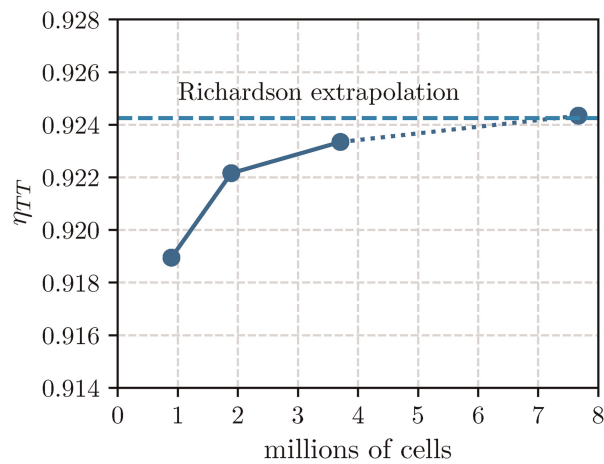


Figure 2. Grid convergence study.

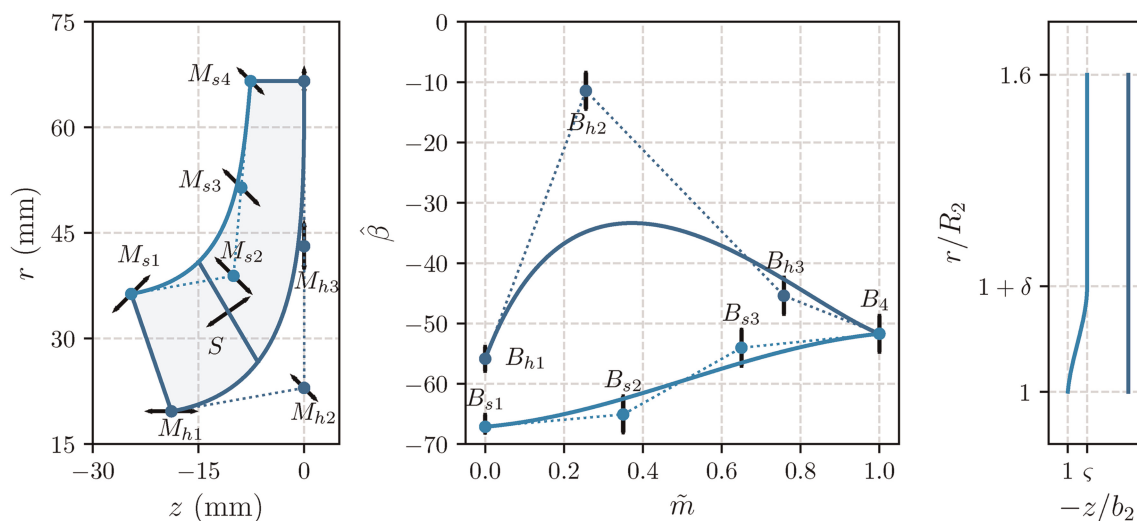


Figure 3. Compressor stage parameterization. (left) meridional channel. (middle) blade angle distribution. (right) vaneless diffuser.

are independent: (i) the trailing edge is cut at the same radial coordinate, therefore the last control point of the hub contour follows the displacement of M_{s4} , and (ii) the outlet blade angle does not change along the span, hence a single control point B_4 is considered for both the hub and the shroud blade-angle distribution. The thickness distribution is not modified throughout the optimization not to compromise the mechanical integrity of the impeller. In general, the splitter blade may follow a different blade angle distribution with respect to the main blade; however, to reduce the number of design variables, the splitter follows the main blade distributions, and the only design parameter is the meridional coordinate at which the main blade is cut (S). Finally, a front pinch is considered for the vaneless diffuser. Correspondingly, the diffuser pinch (ς) and the radial coordinate at which the straight part begins (δ) are both objects of the optimization.

Overall, 17 design variables are considered for the shape optimization problem, of which 7 are related to the meridional channel, 7 control the blade angle distribution, 2 parameterize the vaneless diffuser, and 1 is related to the splitter location. The displacement of each specific control point (horizontal, vertical, or ± 45 deg) is indicated in Figure 3. Table 1 reports the design space for each of these design variables.

Surrogate-assisted evolutionary optimization method

The optimization problem aims to maximize the efficiency, either η_{TT} or η_{TS} , of the stage. Moreover, three constraints are considered, involving the work coefficient λ , the absolute flow angle α_3 at the vaneless diffuser inlet, and the mass imbalance \dot{m}_{imb} of the solution. The choice of the total-to-total efficiency over the total-to-static efficiency depends on whether to consider the whole kinetic energy leaving the vaneless diffuser as a loss. Both objective functions will be considered separately. The first two constraints follow aerodynamic considerations. The work coefficient is constrained because the optimal compressor has to provide the required pressure ratio. An alternative choice would be to constrain the pressure ratio directly. However, as the delivered pressure ratio in the context of sCO₂ compressors is highly dependent on the intake total state, the work coefficient was instead selected to fix the compressor aerodynamic duty. The absolute flow angle cannot exceed 67 deg (measured from the meridional direction) to keep a safe margin from the onset of instabilities in the vaneless diffuser, thus guaranteeing a wide operating range. The flow angle α_3 is always evaluated at $1.2R_2$, which corresponds to the maximum pinch radial extent. If $\delta < 0.2$, the measured angle can slightly differ from the actual value at the diffuser inlet ($r/R_2 = 1 + \delta$) due to viscous effects and density variations. However, both these effects are small owing to the high Reynolds number and the liquid-like properties, respectively, introducing an error of less than 0.2 deg. The last constraint involves the mass imbalance and is included explicitly in the optimization routine to

Table 1. Design space identified by 17 design variables included in the shape optimization.

Meridional channel							
	M_{h1}	M_{h2}	M_{h3}	M_{s1}	M_{s2}	M_{s3}	M_{s4}
Min	-3.0 mm	-2.0 mm	-3.0 mm	-3.0 mm	-3.0 mm	-2.0 mm	-2.0 mm
Max	3.0 mm	2.0 mm	3.0 mm	3.0 mm	3.0 mm	2.0 mm	2.0 mm
Blade angle distributions							
	B_{h1}	B_{h2}	B_{h3}	B_{s1}	B_{s2}	B_{s3}	B_4
Min	-2.0 deg	-3.0 deg	-3.0 deg	-2.0 deg	-3.0 deg	-3.0 deg	-3.0 deg
Max	2.0 deg	3.0 deg	3.0 deg	2.0 deg	3.0 deg	3.0 deg	3.0 deg
Splitter				Vaneless diffuser			
	S			ς	δ		
Min	0.15			0.60	0.10		
Max	0.45			1.00	0.20		

discard solutions that are characterized by a bad convergence. Therefore, the optimization problem reads as:

$$\max \eta_{TT} \quad (\text{or } \eta_{TS}) \tag{1a}$$

$$\text{s.t. } |\lambda - \lambda_{\text{base}}| < 0.005 \tag{1b}$$

$$\alpha_3 < 67 \text{ deg} \tag{1c}$$

$$|\dot{m}_{\text{imb}}| < 0.1\% \tag{1d}$$

The constrained optimization problem is solved with the genetic algorithm (GA). As the GA requires many evaluations to converge, a surrogate strategy is adopted to reduce the computational cost, leveraging the surrogate-assisted strategy implemented in the in-house optimizer FORMA (Persico et al., 2019). At first, 170 stage geometries (ten times the number of design variables) are generated within the prescribed design space with Latin hypercube sampling. The objective function and the constraints are calculated with CFD simulations as detailed in section 2. The mesh is regenerated each time using the grid-convergent set-up described before. Four distinct Kriging, one for each objective function/constraint, are introduced as surrogates of the CFD simulation. The employed Kriging models have up to second-order monomials of the input variables as the mean trend and incorporate a Gaussian correlation function. The Kriging hyperparameters are determined by maximum likelihood optimization. Once the four Kriging predictors are obtained, the GA optimization is executed on surrogate responses. The so-identified optimal stage geometry is assessed with CFD, and new Kriging predictors are re-generated on all simulated cases, namely the initial design of experiments plus the simulated optimal geometries selected by the surrogate optimization. Throughout this acquisition phase, the surrogate reliability progressively increases by adding geometries close to the expected optimal region. The acquisition procedure is repeated for 200 iterations.

A single iteration, which includes surrogate interpolation and optimization, mesh generation, CFD assessment, and post-processing, takes approximately 30 min on a cluster node Dell Intel®Xeon®Gold 6,148 equipped with 40 cores.

Convergence history

The evolution of surrogate estimates for the optimization of η_{TT} and η_{TS} is illustrated in Figures 4 and 5, respectively. These figures depict the convergence after the initial surrogate training on the design of experiments obtained through Latin hypercube sampling. In the initial design pool, no geometries outperform the baseline while satisfying all constraints. Examining the convergence histories, the mass imbalance minimally affects the convergence process. Although a few solutions exhibit appreciable mass imbalance between the inlet and outlet sections, most simulations demonstrate negligible values.

Meeting the targets for λ and α_3 is more critical. The optimization for η_{TS} converges more rapidly, pointing towards the lower limit of $\lambda = 0.620$ and the upper limit of $\alpha_3 = 67$ deg. Conversely, the optimization for η_{TT}

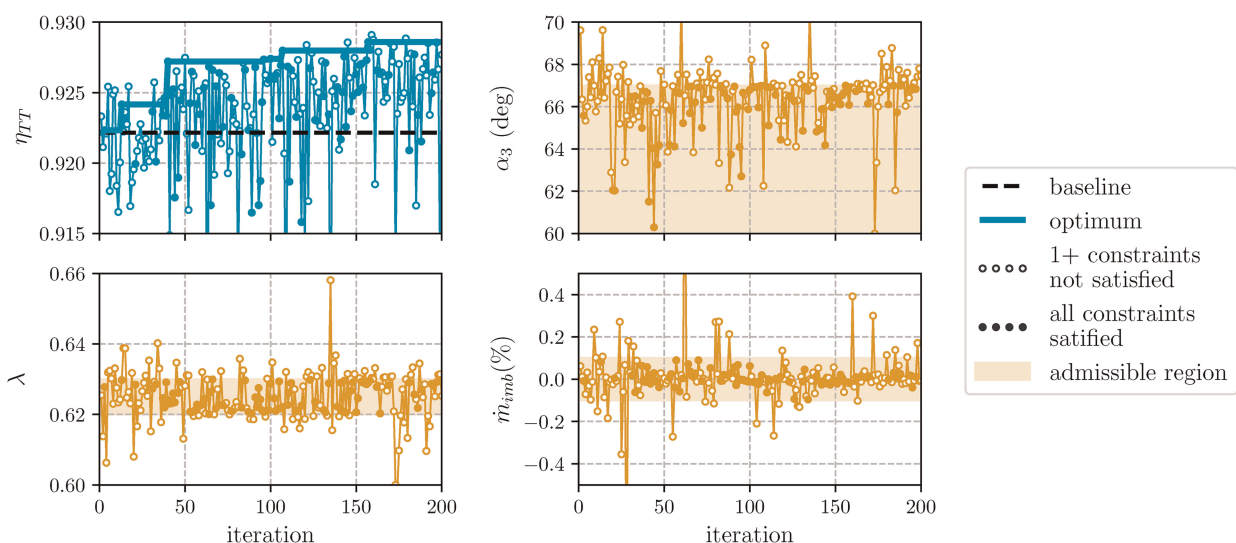


Figure 4. Evolution of surrogate estimates for the total-to-total efficiency maximization.

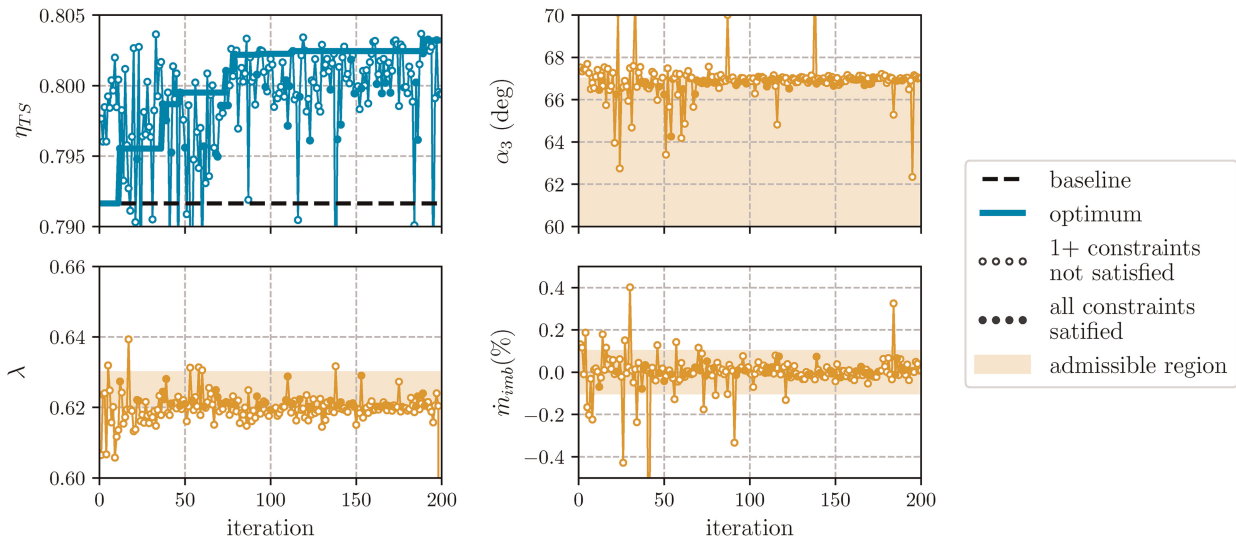


Figure 5. Evolution of surrogate estimates for the total-to-static efficiency maximization.

explores wider variations for the two constraints, possibly indicating multiple optima (multi-modal behavior). Ultimately, the optimal solution maximizing η_{TT} is found close to the upper limit of the α_3 constraint (67 deg).

Both optimization tasks successfully deliver a compressor with improved efficiency while satisfying the imposed aerodynamic constraints. The outlet total and static pressures vary within 1% compared to the baseline value. Maximizing η_{TT} results in a 0.7 percentage point increase (from 92.2% to 92.9%), while maximizing η_{TS} leads to a 1.1 percentage point increase (from 79.2% to 80.3%).

Optimization outcomes

Figure 6 compares the baseline and optimal impeller geometries. On the one hand, starting from the optimization of η_{TT} (optTT), the main changes in the meridional channel are localized at the hub, where the curvature is slightly increased. Then, the backsweep of the blade is reduced, shifting the entire shroud blade angle

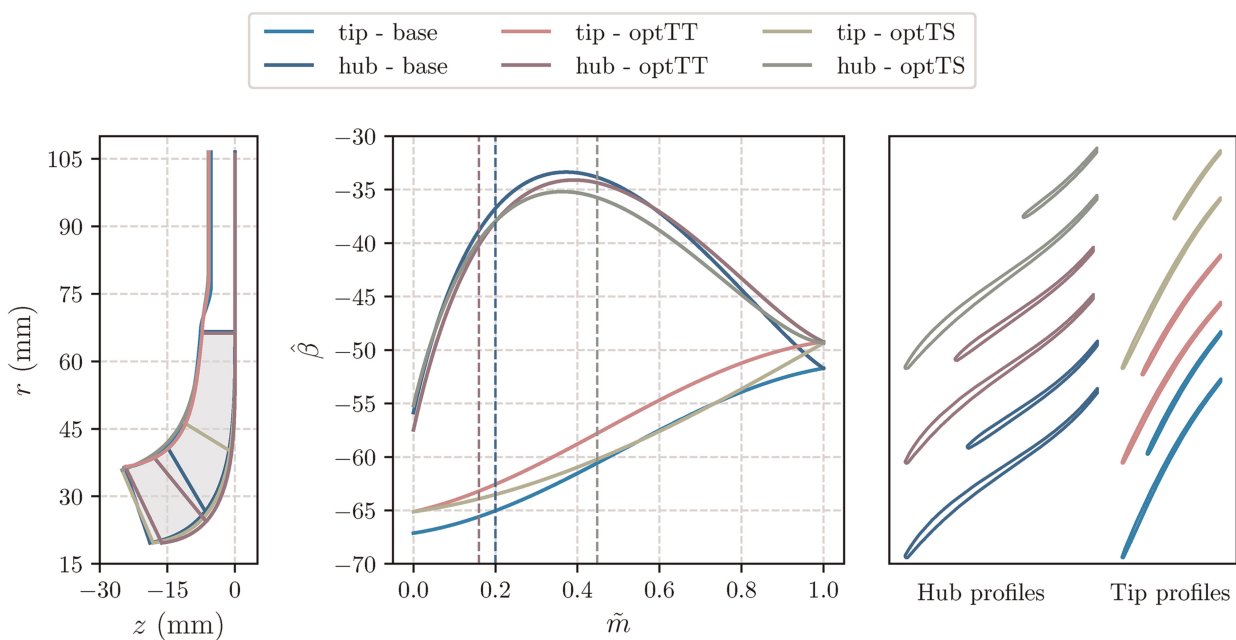


Figure 6. Baseline and optimized impeller geometries. (left) meridional view. (middle) blade angle distribution. (right) blade-to-blade view at hub and tip.

distribution to more meridional values. Moreover, the splitter length is increased to further reduce the aerodynamic loading in the front part of the blade, which has been increased as a consequence of the higher work coefficient. At the same time, the splitter length does not increase the blockage in the impeller inlet area to prevent the onset of choking. It is interesting to note that the optimization has changed the front part of the shroud blade profile, which is typically the most critical region where most of the diffusion occurs.

On the other hand, looking at the optimization of η_{TS} (optTS), different considerations apply compared to the previous case. The meridional channel mirrors the baseline one, but the splitter blade is moved downstream. A partial explanation follows the reduction of the work coefficient. As for the previous optimization, the blade angle distribution at the tip region changed significantly. The outlet blade angle is moved to a more meridional direction, although one would expect the opposite. A more meridional relative flow angle leaving the impeller means higher flow velocity and corresponding skin-friction losses in the vaneless diffuser. At the same time, it also leads to a more tangential absolute flow angle (as highlighted in Figure 5), which increases the effective area ratio of the vaneless diffuser, thus reducing the outlet kinetic energy. Evidently, this latter effect prevails over the former.

The three-dimensional views of the main and splitter blade for the three cases are displayed in Figure 7. The complete list of optimal design variables is reported in Table 2. From this table, it can also be observed that optTT has a vaneless diffuser with a pinched section that extends up to $1.18R_2$ and reduces the outlet channel height by almost 20%. Comparable results are also found for optTS. Interestingly, the optimal values for some variables are found at the extreme boundary of the associated design space, suggesting that there may be space for further improvement by enlarging the design space.

To understand the effect of the optimizations, the Mach number fields near the tip region for the three geometries are reported in Figure 8. Two main flow features can be recognized in the baseline field: first, a flow separation originating on the suction side around $\tilde{m} = 0.2$; second, a limited region of two-phase flow, identifiable by the supersonic Mach number triggered by the drop in the speed of sound (Toni et al., 2022).

The two-phase region is slightly increased for optTT due to the positive incidence resulting from a more meridional inlet blade angle. However, this leads to a considerable reduction in flow detachment on the blade suction side, motivating the optimization path to enhance the total-to-total efficiency. Interpreting optTS is more complex, as the two-phase region considerably enlarges while the separation remains unaltered. This expansion primarily arises from the reduction in splitter length, which contributes to increased blade loading on the main blade. Interestingly, despite these differences, the total-to-total efficiency of optTS matches that of optTT, resulting in a 0.7 percentage point increase over the baseline value. This observation suggests that the optimization problem utilizing η_{TT} as the objective function is multi-modal, with various geometries offering equivalent efficiency values. Therefore, given the same amount of flow separation as the baseline geometry, the total-total efficiency gain for optTS is attributed to the reduction in skin friction loss due to the less wet surface of the splitter blade, offsetting the entropy generation resulting from the separation. In both optimized cases, the diffuser loss amounts to $\omega = 9.1\%$, reduced compared to the baseline case ($\omega = 9.8\%$). However, optTS provides a higher value of η_{TS} compared to optTT, indicating a larger pressure recovery in the diffuser. Specifically, the pressure recovery coefficient is $C_p = 0.50$ for optTS, against 0.49 and 0.48 for optTT and the baseline, respectively. These two optimizations arguably suggest that the total-to-static efficiency can serve as a better formulation of the objective function, as it encompasses entropy generation within the machine similar to the total-to-total efficiency but also considers the kinetic energy leaving the machine.

For a comprehensive compressor performance analysis, it is worthwhile to investigate the variation in the operating range after the optimization. The performance map across the flow range at the nominal rotational speed is depicted in Figure 9. Both the right and left limits are altered due to the optimization. The two optimized cases

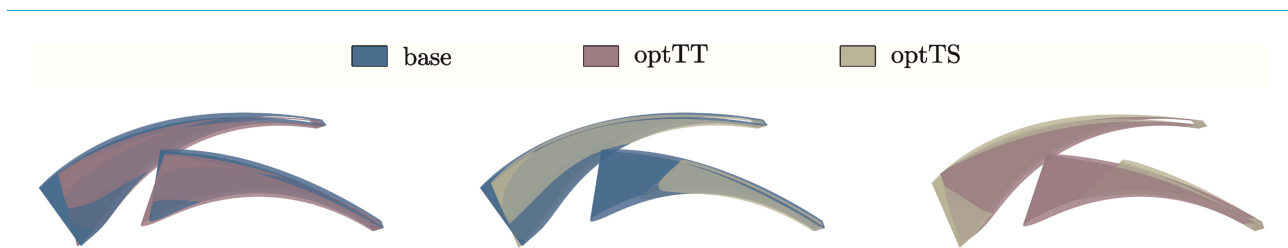


Figure 7. Three-dimensional view of baseline and optimized geometry.

Table 2 Optimal design variables.

	optTT	optTS
M_{h1}	-2.6 mm	-0.7 mm
M_{h2}	-2.0 mm	-0.9 mm
M_{h3}	0.6 mm	-0.2 mm
M_{s1}	0.3 mm	-0.7 mm
M_{s2}	-0.1 mm	2.3 mm
M_{s3}	-1.9 mm	-2.0 mm
M_{s4}	-0.5 mm	-0.5 mm
B_{h1}	-1.6 deg	0.7 deg
B_{h2}	-1.4 deg	-3.0 deg
B_{h3}	0.3 deg	-3.0 deg
B_{s1}	2.0 deg	2.0 deg
B_{s2}	3.0 deg	2.0 deg
B_{s3}	3.0 deg	-3.0 deg
B_4	2.5 deg	2.4 deg
S	0.16	0.45
ς	0.79	0.82
δ	0.18	0.20

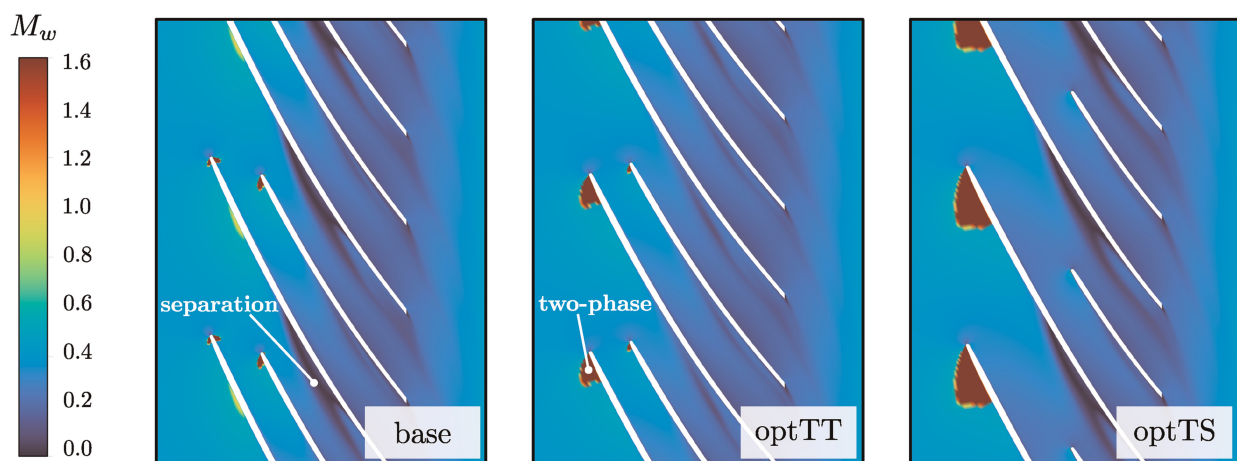


Figure 8. Mach number fields near the tip section for baseline and optimized compressors.

exhibit a similar operating range, shifting towards larger flow rates compared to the baseline. This implies a reduction in the margin from compressor instabilities and an increase in the margin from choked-flow conditions.

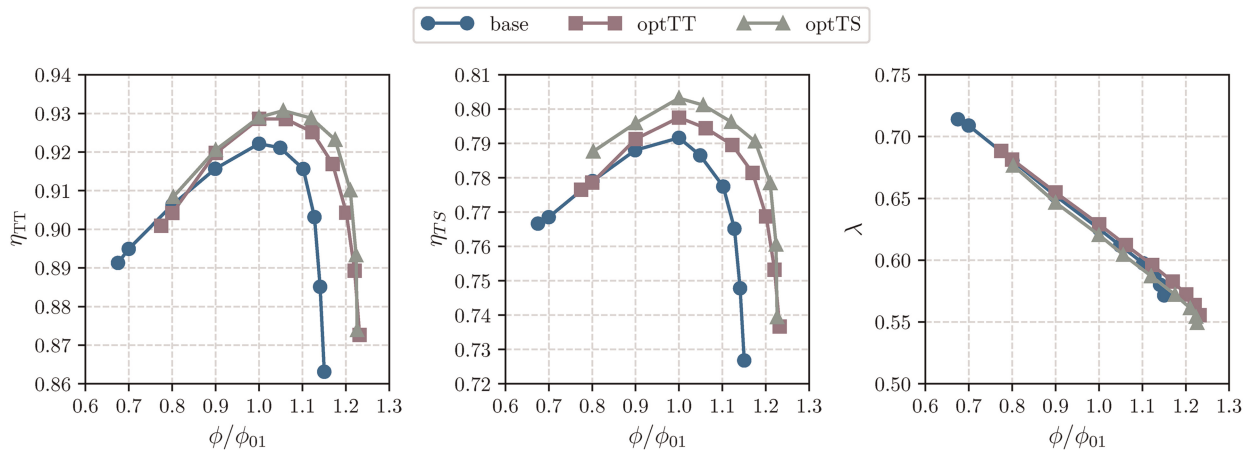


Figure 9. Total-to-total efficiency (left), total-to-static efficiency (middle), and work coefficient (right) curves over the flow range for baseline and optimized geometries.

On the one hand, the left limit, representing the minimum mass flow rate without encountering compressor instability, shifts towards a higher flow rate in the optimized cases by almost 10%. One possible explanation is linked to the absolute flow angle becoming more tangential at the impeller outlet, diminishing the margin from flow instabilities in the vaneless diffuser. It's important to note that identifying the left limit with RANS simulations may be inaccurate, as instabilities are inherently time-dependent phenomena and are also influenced by machine-system interaction. In this analysis, the limit is determined based on numerical considerations, such as when the simulation fails to converge to a steady solution (indicated by oscillations in torque larger than 2%).

On the other hand, the right limit, indicating the maximum mass flow rate before choked-flow conditions occur, increases by 8%. As experimentally demonstrated (Toni et al., 2022), sCO₂ compressors are susceptible to premature choking due to the sudden drop in the speed of sound for the two-phase flow mixture. Choked-flow conditions occur similarly between the baseline and optimized geometries, namely when the two-phase region occupies the entire blade channel at the impeller inlet, establishing the sonic throat. The enhanced swallowing capacity of the compressor results from the larger flow passage area at the throat section, attributed to the increase in hub curvature in the case of optTT and to the reduction in splitter length in the case of optTS.

Conclusion

This work discusses the first attempt at shape optimization for an sCO₂ centrifugal compressor stage. The baseline stage consists of a single stage that yields an overall pressure ratio of approximately 3, starting from the upstream total conditions $P_{01} = 85$ bar and $T_{01} = 305$ K. The baseline shape is parameterized with several Bezier curves for the meridional contours and the blade angle distributions. Additionally, the geometrical parameterization includes the length and extent of the vaneless diffuser pinch, along with the initial splitter meridional location, resulting in a total of 17 design variables.

The shape optimization method is applied to enhance the baseline efficiency while constraining the work coefficient and the absolute flow angle at the impeller outlet. Both total-to-total and total-to-static efficiencies are considered as objective functions. In both cases, the optimization converges to a new compressor shape that is more efficient and satisfies the imposed constraints. Optimizing for total-to-static efficiency yields a substantial increase of 1.1 percentage points, along with a 0.7 percentage point increase in total-to-total efficiency. This efficiency enhancement is achieved by reducing skin friction loss in the impeller through the reduction of splitter blade length and improving the vaneless diffuser. Optimizing for total-to-total efficiency results in the same 0.7 percentage point increase in total-to-total efficiency, albeit with a smaller improvement of 0.6 percentage points in total-to-static efficiency. In this scenario, the improvement is achieved by modifying the blade channel to suppress flow separation at the tip, while also enhancing the vaneless diffuser, albeit with a lower pressure recovery coefficient compared to the optimized geometry for total-to-static efficiency.

As a side effect of both optimizations, the operating range of the compressor changes, with a reduction in surge margin and an increase in the choking limit. This finding suggests the potential for future optimizations that encompass both design and off-design operating points in defining the objective function and constraints.

Nomenclature

α	absolute flow angle
$\hat{\beta}$	blade angle
δ	diffuser pinch
ρ	density
$\eta_{TS} = (h(P_4, s_1) - h(P_{01}, s_1))/l$	total-to-static efficiency
$\eta_{TT} = (h(P_{04}, s_1) - h(P_{01}, s_1))/l$	total-to-total efficiency
μ	dynamic viscosity
$\lambda = l/u_2^2$	work coefficient
$\phi_{01} = \dot{m}/(\rho_{01}u_2D_2^2)$	flow coefficient
$\phi_2 = v_2\cos\alpha_2/u_2$	outlet flow coefficient
ζ	diffuser height reduction
$\omega = (P_{02} - P_{04})/(P_{02} - P_2)$	total pressure loss in the diffuser
b	blade height
B_s	Bezier control point for the shroud blade angle distribution
B_h	Bezier control point for the hub blade angle distribution
c	speed of sound
$C_p = (P_4 - P_2)/(P_{02} - P_2)$	pressure recovery coefficient
h	specific enthalpy
l	eulerian work
M_s	Bezier control point for the shroud meridional contour
M_h	Bezier control point for the hub meridional contour
$M_u = u_2/c_{01}$	peripheral Mach number
\tilde{m}	normalized meridional coordinate
\dot{m}_{imb}	mass imbalance
P	pressure
R	radius
r	radial coordinate
S	splitter location (equivalent to \tilde{m}_{spl})
s	specific entropy
T	temperature
t	thickness
z	axial coordinate
$(\cdot)_1$	impeller inlet
$(\cdot)_2$	impeller outlet
$(\cdot)_3$	diffuser inlet
$(\cdot)_4$	diffuser outlet
$(\cdot)_{0x}$	total quantity
CFD	computational fluid dynamic
HEM	homogeneous equilibrium model
RANS	Reynolds-averaged Navier Stokes
sCO ₂	supercritical carbon dioxide

Funding sources

This work was supported by the CO2OLHEAT project, which has received funding from the European Union's Horizon 2020 research and innovation programme under grant agreement N° 101022831.

Competing interests

Alessandro Romei declares that he has no conflict of interest. Paolo Gaetani declares that he has no conflict of interest. Giacomo Persico declares that he has no conflict of interest.

References

- Ameli A., Turunen-Saaresti T., and Backman J. (2018). Numerical investigation of the flow behavior inside a supercritical CO₂ centrifugal compressor. *Journal of Engineering for Gas Turbines and Power*. 140 (12): 122604. <https://doi.org/10.1115/1.4040577>.
- Baert L., Chérière E., Sainvitu C., Lepot I., Nouvellon A., and Leonardon V. (2020). Aerodynamic optimization of the low-pressure turbine module: exploiting surrogate models in a high-dimensional design space. *Journal of Turbomachinery*. 142 (3): 031005. <https://doi.org/10.1115/1.4046232>.
- Baltadjiev N. D., Lettieri C., and Spakovszky Z. S. (2015). An investigation of real gas effects in supercritical CO₂ centrifugal compressors. *Journal of Turbomachinery*. 137 (9): 091003. <https://doi.org/10.1115/1.4029616>.
- Casey M. and Robinson C. (2021). *Radial Flow Turbocompressors: Design, Analysis, and Applications*. Cambridge University Press.
- Ghimire S., Holder J., Ha M., and Turner M. (2024). Design and optimization of a 3-stage axial supercritical CO₂ compressor. In *The 8th International Supercritical CO₂ Power Cycles Symposium*.
- Hacks A., Schuster S., Dohmen H. J., Benra F. K., and Brillert D. (2018). Turbomachine design for supercritical carbon dioxide within the sCO₂-HeRo.eu project. *Journal of Engineering for Gas Turbines and Power*. 140 (12): 121017. <https://doi.org/10.1115/1.4040861>.
- Hehn A., Mosdzien M., Grates D., and Jeschke P. (2018). Aerodynamic optimization of a transonic centrifugal compressor by using arbitrary blade surfaces. *Journal of Turbomachinery*. 140 (5): 051011. <https://doi.org/10.1115/1.4038908>.
- Hosangadi A., Liu Z., Weathers T., Ahuja V., and Busby J. (2019). Modeling multiphase effects in CO₂ compressors at subcritical inlet conditions. *Journal of Engineering for Gas Turbines and Power*. 141 (8): 081005. <https://doi.org/10.1115/1.4042975>.
- Hosangadi A., Weathers T., Liu J., Pelton R., Wygant K., and Wilkes J. (2022). Numerical predictions of mean performance and dynamic behavior of a 10 MWe SCO₂ compressor with test data validation. *Journal of Engineering for Gas Turbines and Power*. 144 (12): 121019. <https://doi.org/10.1115/1.4055532>.
- Lettieri C., Baltadjiev N., Casey M., and Spakovszky Z. (2012). Low-flow-coefficient centrifugal compressor design for supercritical CO₂. *Journal of Turbomachinery*. 136 (8): 081008. <https://doi.org/10.1115/1.4026322>.
- Lettieri C., Yang D., and Spakovszky Z. (2015). An investigation of condensation effects in supercritical carbon dioxide compressors. *Journal of Engineering for Gas Turbines and Power*. 137 (8): 082602. <https://doi.org/10.1115/1.4029577>.
- Pecnik R., Rinaldi E., and Colonna P. (2012). Computational fluid dynamics of a radial compressor operating with supercritical CO₂. *Journal of Engineering for Gas Turbines and Power*. 134 (12): 122301. <https://doi.org/10.1115/1.4007196>.
- Pelton R., Jung S., Allison T., and Smith N. (2018). Design of a wide-range centrifugal compressor stage for supercritical CO₂ power cycles. *Journal of Engineering for Gas Turbines and Power*. 140 (9): 092602. <https://doi.org/10.1115/1.4039835>.
- Persico G., Rodriguez-Fernandez P., and Romei A. (2019). High-fidelity shape optimization of non-conventional turbomachinery by surrogate evolutionary strategies. *Journal of Turbomachinery*. 141 (8): 081010. <https://doi.org/10.1115/1.4043252>.
- Rinaldi E., Pecnik R., and Colonna P. (2015). Computational fluid dynamic simulation of a supercritical CO₂ compressor performance map. *Journal of Engineering for Gas Turbines and Power*. 137 (7): 072602. <https://doi.org/10.1115/1.4029121>.
- Romei A., Gaetani P., and Persico G. (2023). Guidelines for the aerodynamic design of sCO₂ centrifugal compressor stages. *Journal of Engineering for Gas Turbines and Power*. 145 (11): 111014. <https://doi.org/10.1115/1.4063311>.
- Toni L., Bellobuono E. F., Valente R., Persico G., Romei A., and Gaetani P. (2022). Computational and experimental assessment of a MW-scale supercritical CO₂ compressor operating in multiple near-critical conditions. *Journal of Engineering for Gas Turbines and Power*. 144 (10): 101015. <https://doi.org/10.1115/1.4055364>.
- Verstraete T., Alsalihi Z., and Van den Braembussche R. A. (2010). Multidisciplinary optimization of a radial compressor for microgas turbine applications. *Journal of Turbomachinery*. 132 (3): 031004. <https://doi.org/10.1115/1.3144162>.